applied optics

Application of Mie theory for enhanced size determination of microparticles using optical particle counters

Dennis Müller,* Felix Glöckler, and Alwin Kienle

Institute for Laser Technologies in Medicine and Metrology (ILM), Helmholtzstr. 12, 89081 Ulm, Germany
**Corresponding author: dennis.mueller@ilm-ulm.de*

Received 1 April 2019; revised 14 May 2019; accepted 14 May 2019; posted 15 May 2019 (Doc. ID 363984); published 4 June 2019

The approach to particle sizing with optical particle counters is often simple interpolation of calibration data. A method is presented that uses the results of Mie-theory-based simulations to describe the signal between calibration points, thus reducing the number of necessary calibration points or increasing the sizing accuracy significantly. Through the use of Mie theory, particles with a refractive index differing from the calibration particles can be measured without an individual calibration. The method can be used with custom research setups or commercially available optical particle counters with various detector designs. If needed, the method can be applied to particle counters for which only the light wavelength used is known. The method is tested using a commercially available optical particle counter with a polystyrene microsphere calibration, measuring polystyrene microspheres as well as THP-1 cells, Chinese hamster ovary cells, and yeast cells. Without material specific calibration, simple interpolation results in about half the actual particle sizes for these biological samples, whereas the presented method yields accurate results.

https://doi.org/10.1364/AO.58.004575

1. INTRODUCTION

The quantitative determination of particle concentrations and sizes has reached enormous significance over the past years. Particle counting techniques are used in environmental [1] and biological [2,3] applications as well as in industrial processes. Their employment ranges from the detection of aerosol particles in forests [4] to counting dust particles in clean room facilities [5]. Particle counting techniques are used to monitor debris particles [6] in lubricants and contamination in water purification [7,8]. Biomedical applications use particle counters, for example, to detect single DNA molecules [9,10] and DNA content [11]. Particle counters are also used for diagnostic purposes, i.e., counting white blood cells [12–15], which is vital for a variety of applications, such as the detection of HIV infections [16].

Of particular interest in this field are extinction (light-blocking) sensors due to the high accessible sample flow rates and their relatively simple design. Alienable products are mostly calibrated with a single particle standard to assign sizes to certain signal strengths, thus yielding wrong results for particles with differing refractive index.

In this work we present a method for enhanced particle diameter determination that can be applied post-measurement or integrated in already established in-line techniques. The enhancement is achieved by consideration of light scattering effects described by Mie theory [17] during interpolation of the measurement data. Mie theory has been used in scientific particle sizing before, in combination with a light scattering microscope [18–20], Mie resonance spectroscopy [21], laser diffraction spectroscopy [22], and various other measurement methods [23–26], but has not yet been introduced to measurement data interpretation of optical particle counters.

The Mie-theory-based interpolation allows for a lower count of calibration points, reducing time and financial costs of the calibration procedure, while increasing the diameter determination accuracy of the setup. Furthermore, the presented method allows measurement of particles with a material differing from the calibration material without individual calibration.

The method was tested with a commercially available particle counter. First, the calibration improvement on polystyrene microspheres is shown. Second, using the polystyrene calibration from before, measurements on biological samples are presented.

2. METHOD

Counting microparticles is often achieved using light scattering by single particles that move through a sufficiently small detection volume to avoid particle coincidences. Light scattering setups detect the scattered light directly at certain scattering angles, while extinction sensor setups have their sensors

positioned inside the path of the unscattered light and are, therefore, sensitive to the portion of the light that is scattered away from the sensor. Particle sizes can be correlated to the amount of light scattered by the particle. The established method for particle size determination in commercial products is the interpolation of calibration data obtained by reference particles, for example, linear or piecewise cubic. The performance of this method depends strongly on the smoothness of the calibration curve and on the number of calibration points.

Figure 1(a) shows two calibration curves. Both are calculated from the same calibration data for a Syringe particle counter, which is explained in detail at the end of this section. The blue curve is obtained by piecewise cubic interpolation of the calibration data and is therefore as featureless as possible between the calibration points, while conserving the continuity of the curve and its derivative at the calibration points. The red curve is calculated using Mie-theory-based simulations of the light scattering on spherical particles of different sizes with the refractive index of the calibration material. This curve clearly shows significant features between calibration points representing the light scattering behavior of spherical particles of the calibration material. To consider these features using piecewise cubic interpolation, the feature would have to be sampled with numerous calibration points. Mie-theory-based interpolation, on the other hand, uses knowledge from simulations to correctly predict the irregularities in the light scattering signals between calibration points and conclude the correct particle sizes.

The common approach to particle size determination makes it also necessary to calibrate the setup for each material studied. Figure 1(b) shows the differing theoretical extinction sensor signals for particles of various materials. In the case of biological samples, finding suitable calibration standards can be difficult. Since the presented method is based on Mie theory, which includes the refractive index (RI) of the scatterer, additional calibrations are not needed—only the refractive index has to be known. This is also true for studies of particles in different surrounding media.

The measured sensor output of the commercial particle counter is denoted U_{meas} and, in the case of the presented setup, is represented in units of volts. In the common approach, the measured diameters D_{meas} are obtained by interpolation of the sensor output values U_{meas} and the calibration data, a set of corresponding sensor output values U_{calib} and diameters D_{calib}, as depicted in Fig. 1(c).

The approach including Mie theory allows calibration improvements and a direct correction of particle diameters for different materials. Mie-theory-based light scattering simulations, which are represented by the blue dashed boxes in Fig. 1, yield light power values, while only output voltages U_{meas} are obtainable from a commercial setup without applying probes inside the detector electronics. To obtain the light power measured by the sensor, the inverse of the setup response function $P(U)$ has to be known or approximated. This can be done using the calibration data and will be explained later in detail (see Section 2.4). With the inverse setup response function, the sensor output can be translated into light power values P_{meas} detected by the sensor. These can be compared with powers P_{sim} from the Mie-theory-based simulations to obtain the corresponding corrected particle diameters, as presented in Fig. 1(d). This approach can be used to generate a new calibration curve for the setup, linking sensor output signals U_{meas} with the corrected diameter values D_{corr} for particles of any material with a known refractive index n_{meas}.

The calculation of the simulated power P_{sim} can be divided into three parts: first, the light scattering of the particle; second, the possible influences of a microfluidics cuvette; and last, the influences of the sensor, which will be described in Sections 2.A, 2.B, and 2.C, respectively. Section 2.D describes the approximation of the inverse setup response function $P(U)$.

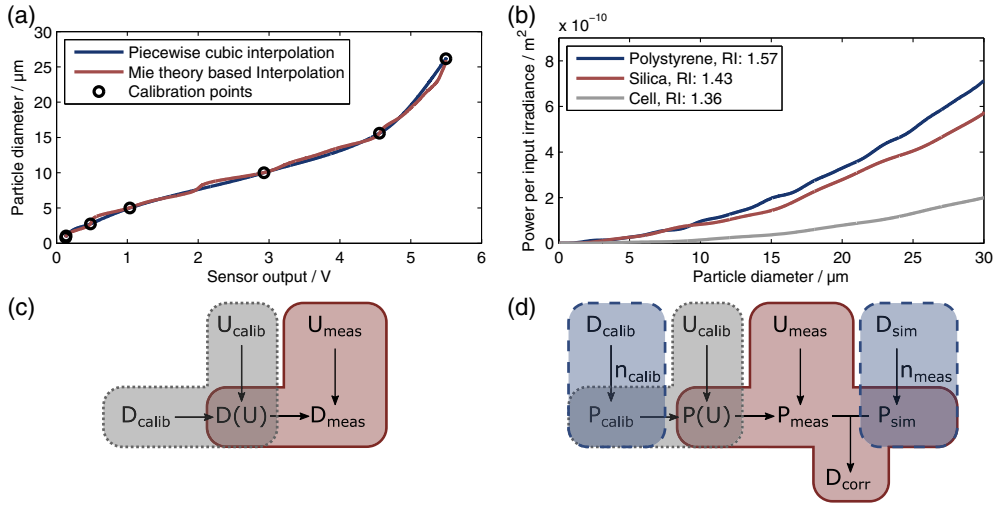

Fig. 1. (a) Two calibration curves for an extinction sensor setup. The blue one is derived by piecewise cubic interpolation of the calibration data, represented by the circled calibration points. The red curve uses the same calibration data but is based on Mie theory simulations, thereby considering the scattering behavior of the analyzed scatterers. (b) The scattering signal for particles with various refractive indices. (c) The common approach of particle size determination, followed by (d) the presented method, which extends the common approach by implementation of Mie-theory-based simulation data, marked by the blue dashed boxes.

The following calculations are performed for a commercially available particle counter (Syringe, Markus Klotz GmbH, Germany) that is later on used to test the presented method. This particle counter uses an extinction sensor and an illumination wavelength of 780 nm. Further parameters of the setup, such as the cuvette geometry, are described below.

A. Light Scattering Simulation

All particles considered in the presented work are assumed to be spherical, therefore rotational symmetry can be assumed in the light scattering simulations. Using Mie theory [17], as described in Bohren's and Huffman's "Absorption and Scattering of Light by Small Particles" [27], Mueller matrices M can be calculated for various scattering angles θ. As truncation criterion N_t for the infinite series expansion of the Mie theory solutions,

$$N_t = \lceil x + 4.05x^{\frac{1}{3}} + 2 \rceil \quad \text{with } x = \frac{2\pi n_m}{\lambda}, \tag{1}$$

was used in accordance with Wiscombe's findings [28]. The parameter n_m describes the medium refractive index, while the wavelength is denoted by λ. Other parameters influencing the simulated light scattering are the sphere diameter D_{sim} and the scatterer refractive index n_s. These Mueller matrices transform an incoming Stokes vector [29] into an outgoing one that describes the scattered intensities $I_{\text{out}}(\theta)$ and corresponding polarizations via $Q_{\text{out}}(\theta)$, $U_{\text{out}}(\theta)$, and $V_{\text{out}}(\theta)$:

$$\begin{pmatrix} I_{\text{out}}(\theta) \\ Q_{\text{out}}(\theta) \\ U_{\text{out}}(\theta) \\ V_{\text{out}}(\theta) \end{pmatrix} = \frac{1}{k^2 r^2} M(\theta) \cdot \begin{pmatrix} I_{\text{in}} \\ Q_{\text{in}} \\ U_{\text{in}} \\ V_{\text{in}} \end{pmatrix}. \tag{2}$$

The variable k describes the wavenumber, while r represents the distance at which the intensity is measured. Integrating these intensities over corresponding elements of a spherical surface with radius r eliminates the distance and results in the light power P that is scattered into the solid angle belonging to the scattering angle θ:

$$P(\theta) = 2\pi r^2 \sin(\theta) \Delta\theta I_{\text{out}}(\theta), \tag{3}$$

$$\frac{P(\theta)}{I_{\text{in}}} = \frac{2\pi}{k^2} \sin(\theta) \Delta\theta M(\theta) \cdot \begin{pmatrix} 1 \\ 0 \\ 0 \\ 0 \end{pmatrix}. \tag{4}$$

Since the input irradiance I_{in} is not necessarily known and nonpolarized illumination is used, division yields the diverted power per input irradiance, which therefore is measured in the units of an area. The factor $2\pi \sin(\theta)$ in Eqs. (3) and (4) originates from the already executed integration of the azimuthal angle ϕ in combination with the rotational symmetry of the problem. The angular resolution of the scattering angle in the Mie-theory-based simulation is denoted by $\Delta\theta$.

Integration to obtain power per solid angle has two advantages. The first is that the distance between the scatterer and the detector is irrelevant, since the power inside the solid angle is conserved in vacuo. The second is that the angle under which the light is detected by the sensor is irrelevant as well, for any increase in detection area over which the intensity would spread is handled through the scattering angles. A tilted sensor will detect fewer scattering angles than an orthogonally orientated one and thus will sense less power.

B. Cuvette Influences

Some aerosol particle counters do not use a cuvette in their setup. In those cases, this section can be skipped and the effective scattering angle θ_{eff} in the later sections is to be replaced with the actual scattering angle θ.

Figure 2(a) shows the schematic of the cuvette of the setup used. Two glass slabs are held in place by a metal retainer, creating a defined space between the glass slabs, in which the medium carrying the particles can flow. Disregarding the influence of the metal sidewalls, rotational symmetry is conserved. The incident light passes the first glass slab orthogonally, enters the medium, and is scattered by a particle. The scattered light passes the second glass slab at various angles, as depicted in Fig. 2(b). The scattering angle leading to total reflection θ_{tr} at the glass–air interface of the second glass slab is easily determined by

$$\theta_{\text{tr}} = \arcsin\left(\frac{1}{n_{\text{m}}}\right). \tag{5}$$

Neglecting light paths with more than one interaction per glass interface, scattering angles greater than θ_{tr} will not leave the cuvette toward the sensor and therefore cannot be detected. All other scattering angles lead to light paths that leave the cuvette toward the sensor. With known widths of the medium d_m, the glass d_g, and the sensor d_s, these lateral offsets from the optical axis at the sensor plane can be calculated with the use of Snellius' laws. From this offset, an effective scattering angle θ_{eff} can be assigned to each actual scattering angle θ:

$$\theta_{\text{eff}}(\theta) = \arctan\left(\frac{\frac{d_m}{2}\tan(\theta) + d_g \tan\left(\arcsin\left(\frac{n_m}{n_g}\sin(\theta)\right)\right) + d_s \tan\left(\arcsin\left(\frac{n_m}{n_s}\sin(\theta)\right)\right)}{\frac{d_m}{2} + d_g + d_s}\right). \tag{6}$$

The transmission and reflection at the glass interfaces in accordance with Fresnel's equations can also be handled in the Mueller–Stokes formalism [30]. To incorporate the polarization of the scattered light correctly, transmission and reflection have to be applied before the integration from Eqs. (3) and (4).

The particle counter setup used in this study has an extinction sensor that is exposed to the complete input irradiance when there is no particle inside the illuminated volume.

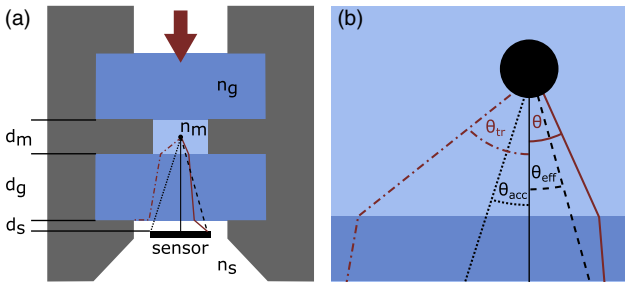

Fig. 2. (a) Schematic of the cuvette of the setup, as well as (b) an overview of the most significant light paths. The angle θ represents the actual scattering angle, θ_{eff} the effective scattering angle, θ_{tr} the scattering angle of total reflection, and θ_{acc} the acceptance angle of the sensor with respect to the effective scattering angle θ_{eff}.

As a particle enters the volume, light is scattered away from the sensor. Through a high pass filter, the sensor acts in a near differential manner, only outputting the rapid changes of detected power due to particles passing through the detection volume. Thus, all light not hitting the sensor has to be integrated to obtain the signal the sensor detects. It is therefore of no importance in this setup configuration whether the light power is not detected due to missing the sensor surface or due to reflection at the glass slab interfaces. Hence, the reflected and transmitted portions of light paths not hitting the sensor do not need to be calculated. The reflected portion of the light hitting the sensor, on the other hand, influences the output signal. The reflectance matrix R_0 with no particle present can be described by the reflectance matrices of the first glass interface R_1 and the second one R_2 for orthogonal incidence:

$$R_0 = R_2(\theta)|_{\theta=0}(1 - R_1(\theta)|_{\theta=0}) + R_1(\theta)|_{\theta=0}. \tag{7}$$

With a particle present, non-orthogonal light paths passing the cuvette glass surfaces are possible, as depicted in Fig. 3(a).

Since the high pass basically subtracts the state of the sensor with no particle present, for calculations of the signal with a particle inside the measurement volume the reflectance R_0 has to be subtracted. The combined reflectance R of both glass slab interfaces can be calculated, the reflectance without a particle R_0 subtracted, and the intensities I_{sens} for light hitting the sensor determined, which replace I_{out} in Eq. (3):

$$R_\Delta(\theta) = R(\theta) - R_0 = R_2(\theta) \cdot (1 - R_1(\theta)) + R_1(\theta) - R_0, \tag{8}$$

$$S_{\mathrm{sens}}(\theta) = R_\Delta(\theta) \cdot S_{\mathrm{out}}(\theta), \tag{9}$$

$$I_{\mathrm{sens}}(\theta) = R_{\Delta(1,1)}(\theta) I_{\mathrm{out}}(\theta) + R_{\Delta(1,2)}(\theta) Q_{\mathrm{out}}(\theta). \tag{10}$$

For spherical particles in combination with a non-polarized illumination, U_{out} and V_{out} are always equal to 0, resulting in the simplified Eq. (10). Figure 3(b) shows that the first two elements of the first column of the differential reflectance matrix R_Δ are sufficiently small to be neglected for the presented extinction sensor setup, where only effective scattering angles up to 5.6° can hit the sensor. Other setups, especially scattering light sensors with high angles toward the cuvette glass surface, have to regard these influences in order to assess the correct particle sizes.

C. Sensor Influences

To decide which effective scattering angles θ_{eff} hit the sensor, an effective acceptance angle θ_{acc} can be determined, as shown in Fig. 2(a):

$$\theta_{\mathrm{acc}} = \tan\left(\frac{r_{\mathrm{sens}}}{d_{\mathrm{sens}}}\right), \tag{11}$$

with r_{sens} being the radius of the sensor, and d_{sens} the distance of the sensor from the most probable particle location. The condition for light from a scattering angle θ to not hit the sensor is easily described in the case of a round sensor geometry:

$$\theta_{\mathrm{eff}} > \theta_{\mathrm{acc}}. \tag{12}$$

At first glance, a square sensor disrupts the assumed rotational symmetry of the problem. The solution is to determine the parts of concentric circles that lie outside a square, since the light not hitting the sensor has to be found for this detector setup. This problem has an eightfold symmetry. Finding the intersection of a circle and a side of the square yields an azimuthal angle ϕ, as depicted in Fig. 4(a).

The ratio of the circumference lying outside the square ΔC is then described by

$$\Delta C = \frac{4\phi}{\pi}. \tag{13}$$

This ratio can be used as a weighting function for the effective scattering angles θ_{eff}:

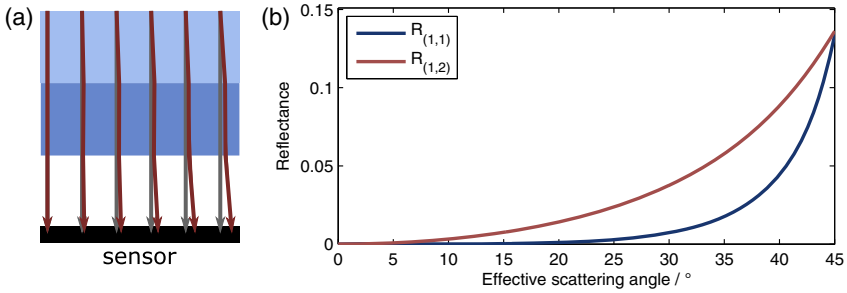

Fig. 3. (a) Introduction of non-orthogonal light paths to the cuvette surfaces through the presence of a particle in the detection volume. The reflectance of the interfaces changes with these angles. This effect is shown in (b), which presents the two most important elements of the reflectance matrix when studying spherical scatterers.

$$w(\theta_{\mathrm{eff}}) = \frac{4\phi(\theta_{\mathrm{eff}})}{\pi} = \frac{4}{\pi}\arccos\left(\frac{r_{\mathrm{sens}}}{2d_{\mathrm{sens}}\,\tan(\theta_{\mathrm{eff}})}\right). \quad (14)$$

The radius of the sensor r_{sens} is defined by half of the diagonal of the square sensor, since this point accepts the highest scattering angles. The weighting functions for a round and a square sensor are shown in Fig. 4(b) for an exemplary effective acceptance angle of 7°. Additionally the trivial cases, where the full circle for θ_{eff} lies either inside or outside the sensor surface are defined as

$$w\left(\theta_{\mathrm{eff}} < \arctan\left(\frac{r_{\mathrm{sens}}}{\sqrt{2}d_{\mathrm{sens}}}\right)\right) = 0, \quad (15)$$

$$w(\theta_{\mathrm{eff}} > \theta_{\mathrm{acc}}) = 1.$$

The sum over the weighted scattered powers per incident irradiance yields the relative power drop detected by the sensor when a particle is present:

$$\frac{P_{\mathrm{sim}}}{I_{\mathrm{in}}} = \sum_{\theta_{\mathrm{eff}}} w(\theta_{\mathrm{eff}})\frac{P(\theta_{\mathrm{eff}})}{I_{\mathrm{in}}}. \quad (17)$$

With a known and stable input irradiance I_{in}, the simulated power drop on the sensor P_{sim} can be calculated. Since the effect of I_{in} is of linear nature, it can also be easily eliminated during the determination of the inverse setup response function in the subsequent section.

The above calculations have to be performed for a range of particle diameters D_{sim} that includes the assumed diameters of the measured particles. The resulting curve $P_{\mathrm{sim}}(D_{\mathrm{sim}})$ has to be inverted to obtain the corrected diameters D_{corr} from the measured power signals P_{meas}. Therefore, $P_{\mathrm{sim}}(D_{\mathrm{sim}})$ has to be monotonic. Since it contains rapid oscillations for high refractive index and high particle diameters a Savitzky–Golay filter [31] is used. Figure 5(a) shows that the general shape of the simulated signal is not deterred by the application of the Savitzky–Golay filter. A section with rapid oscillations in the simulated signal is enhanced in Fig. 5(b), presenting the smoothing by the filter, rendering the curve monotonic and invertible.

D. Setup Output Signal

To obtain the power detected by the sensor during measurements, the relation between this power and the setup output signal has to be determined. This can be achieved using the calibration data set, consisting of known particle and medium refractive index, particle diameters, and resulting setup output signals. From those parameters, the corresponding detected power drop P_{calib} can be simulated, as shown in Fig. 1(d) and presented in the above sections. This corresponding power values P_{calib} and sensor output signal values U_{calib} can be used to interpolate the power values P_{meas} from the measurement setup output values U_{meas}.

The presented setup uses a high pass filter, which lets the sensor act in a nearly differential fashion. This effect is already handled by calculating the power of the light scattered away from the sensor by the presence of a particle. Still, the setup

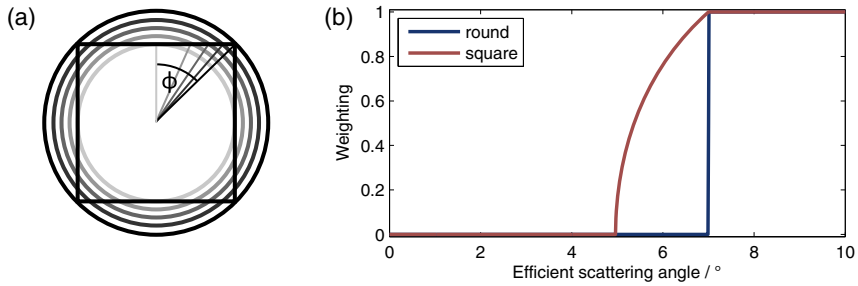

Fig. 4. This figure describes the influences of the sensor shape. (a) A way to determine a weighting function for square sensors to maintain the rotational symmetry of the problem. (b) The influence on the effective scattering angles contributing to the sensor signal for an exemplary effective acceptance angle of 7°.

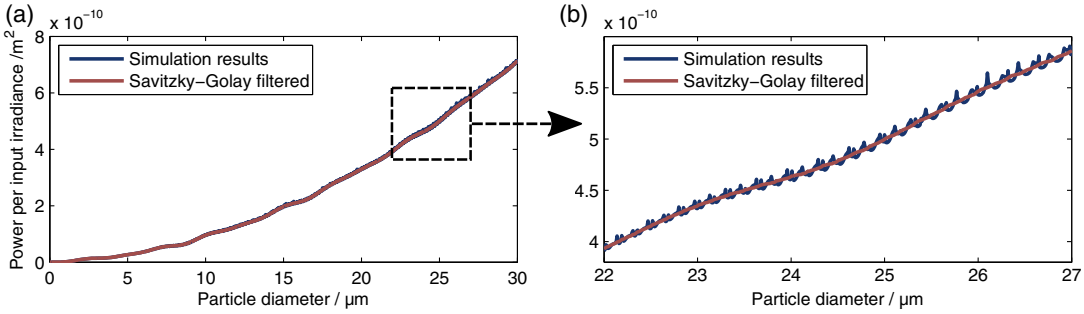

Fig. 5. To make the curve $P(D)$ invertible, it has to be smoothed. This is achieved by applying a Savitzky–Golay filter of the third order. The ripples in the simulated signal introduce a certain degree of uncertainty to the particle diameter determination with an extinction sensor. This effect is inherent with the setup geometry and increases with the particle diameter and the relative refractive index, i.e., the ratio between the refractive index of the scatterer and the refractive index of the medium.

output signal seems to behave nonlinearly in relation to the power drop for the presented setup. This might be caused by the exposure of the sensor to very high intensities, while detecting only slight changes in the detected power. Therefore, we used piecewise cubic interpolation to approximate the input power to output signal curve of the setup.

3. APPLICATION AND DISCUSSION

Putting the method to the test, first the particle counter (Syringe, Markus Klotz GmbH, Germany) was calibrated with a set of polystyrene particles of the sizes shown in Table 1. The particles were suspended in 1 ml of double-distilled water. Disagglomeration was achieved by exposing the suspension container to an ultrasonic bath for 30 min. Subsequently, the suspension was diluted with double-distilled water again to obtain 50 ml of sample suspension. All following anorganic particles were prepared in this manner.

The calibration yields the sensor output signals U_{calib} corresponding to the particle sizes D_{calib}. To obtain the single output signal value U_{calib} for each suspension, a Gaussian function was fitted onto the resulting sensor output signal distribution, and its central signal was labeled U_{calib}. With simulations of the present power drop on the sensor, the power values P_{calib} were calculated, providing the data points for the piecewise cubic interpolation of the inverse setup response function $P(U)$.

Table 1. Manufacturer Information on the Sizes of the Microspheres Used[a]

Calibration Particles/µm	Test Particles/µm
$0.81 \pm 0.04^{(3)}$	$1.50 \pm 0.04^{(2)}$
$1.03 \pm 0.04^{(1)}$	$2.03 \pm 0.04^{(1)}$
$2.74 \pm 0.05^{(1)}$	$2.39 \pm 0.04^{(1)}$
$5.00 \pm 0.07^{(2)}$	$4.21 \pm 0.07^{(1)}$
$10.00 \pm 0.15^{(2)}$	$4.47 \pm 0.07^{(1)}$
$15.59 \pm 0.13^{(1)}$	$19.30 \pm 0.36^{(1)}$
$26.15 \pm 0.36^{(1)}$	–

[a]Polystyrene was used as calibration material. The corresponding particle sizes are listed in the first column of this table. A second set of polystyrene particles was measured to test the improvement of the calibration obtained from the first set. The sizes of the second set are shown in the second column. Manufacturers are marked as follows: (1) microParticles GmbH, Germany, (2) BS-Partikel GmbH, Germany, and (3) Thermo Fisher Scientific (DUKE), USA.

At this point, the setup was characterized and the method could be tested.

First, the calibration improvement was evaluated. Figure 6(a) shows the theoretical relative error in diameter determination induced by piecewise cubic interpolation instead of Mie-theory-based interpolation. To evaluate the performance of both methods, particles of the same material as the calibration set were measured and the sensor output signals were translated into particle diameters using each method. The corresponding particle sizes are listed in Table 1. They were prepared the same way as was the calibration set.

The next evaluation steps were measurements on biological samples, such as THP-1, CHO, and yeast cells. Figure 6(b) shows the theoretical relative error for the size determination of particles with materials differing from the calibration. For a polystyrene calibration, some size ranges exist where measuring other materials results in very similar signals, such as silica microspheres between 5 and 8 µm. Particle size determination of biological samples with refractive index lower than 1.4, on the other hand, yield large errors, as shown by the blue curve of Fig. 6(b).

THP-1 cells and CHO cells were bought in suspension culture, kept in an incubator at 37°C and 5% CO_2, and regularly split to prevent overpopulation. Yeast CY 3079 cells were acquired in a dried state. 5 g of dried yeast cells were brought into a buffer medium, consisting of 10 g of tryptone and 10 g of dextrose, which have been solved in 500 ml of double-distilled water and subsequently cultured in an incubator shaker at 30° C. To prepare the cells for measurement, they were centrifuged and brought into phosphate-buffered saline (PBS). In accordance with Liang *et al.* [32], the difference in refractive index of PBS to water was assumed negligible, so a medium refractive index of 1.33 was used for cell measurements, as well.

Su *et al.* [34] have compared measurements of THP-1 cells with numerical simulations. They assumed the refractive index of the cytoplasm to be 1.35, of the nucleus to be 1.39, and of the mitochondria to be 1.42 at a wavelength of 532 nm. Therefore, we assumed an effective refractive index for a THP-1 cell of 1.37 at a wavelength of 543 nm and 1.36 at 780 nm, which is used by the presented setup. They assumed a particle diameter of 12 µm in accordance with Tsuchiya *et al.* [37], who found cell sizes to be between 12 and 14 µm. Using phase contrast microscopy, the size distribution of the analyzed THP-1 cells was determined to reach from 10 µm to 18 with large numbers of cells between 11 and 13 µm. A representative

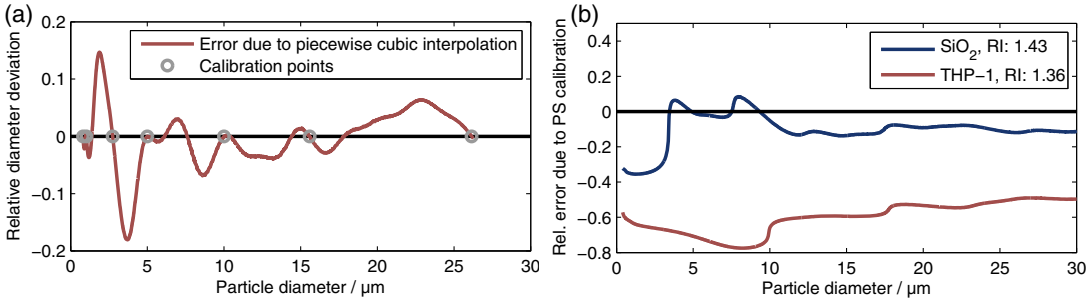

Fig. 6. Two major applications of the presented method are shown in this figure. (a) The theoretical relative error for determined particle diameters due to the usage of piecewise cubic interpolation. (b) The theoretical relative error in diameter determination, when measuring particles, disregarding differing refractive indices in the calibration and measurement process. The assumed calibration material in (b) was polystyrene.

Table 2. Parameters Assumed for the Analyzed Cells, based on Phase Contrast Microscopy Measurements (See Fig. 8) and the Works of Choi *et al.* [33], Su *et al.* [34,35], and Stark *et al.* [20,36]

	THP-1	CHO	Yeast
Size distribution/µm	(10)**11**–1**3**(18)	(11)**12**–**15**(18)	(4)**5**–7(8)
Assumed particle RI	1.360	1.360	1.385

fraction of the microscopic images is shown in the results section in Fig. 8. Chinese hamster ovary cells (CHO) have been studied in our group before [36]. In accordance with Su *et al.* [35], the refractive index of the cytoplasm was assumed to be 1.36, of the nucleus to be 1.39, and of the mitochondria to be 1.38 at a wavelength of 405 nm. Regarding the low wavelength for which the above values have been determined, we assumed an effective refractive index of 1.36, as well. The size distribution for analyzed CHO cells was determined to range from 11 to 18 µm. Cells with a size of 12 µm have been found most frequently, with a relatively equal distribution between cell sizes from 13 to 15 µm and a low population of cell sizes above 15 µm. Previous works on CY 3079 yeast cells by our group [20] found that Mie-theory-based simulations with an effective refractive index of 1.40 at a wavelength of 543 nm approximate goniometric measurements of said yeast cells well. For a wavelength of 780 nm, we assumed a refractive index of 1.385. The particle size distribution was determined to range from 4 to 8 µm with its peak at 6 µm, with a gradually decreasing population of cell sizes in both directions.

4. RESULTS

A. Calibration Improvement

The first set of measurements concerned the polystyrene calibration improvement. By linear or piecewise cubic interpolation between calibration points, significant fluctuations in scattering intensities are lost, which can be described using Mie theory. Figure 7 shows the results for polystyrene microsphere measurements with a polystyrene calibrated setup. The results for piecewise cubic interpolation in the calibration data is represented by the blue curves, while the Mie-theory-based interpolation is depicted in red. The manufacturer information is shown by the vertical black solid line, with the margin of error indicated as the dashed lines. All results contain various small peaks that are already contained in the sensor output signal U_{meas} and are therefore considered artifacts of the experimental setup.

Figure 7 shows the improvement in sizing accuracy clearly, particularly for particles between 2 and 5 µm. While the particle size distributions from simple interpolation have very little overlap with the values given by the manufacturers,

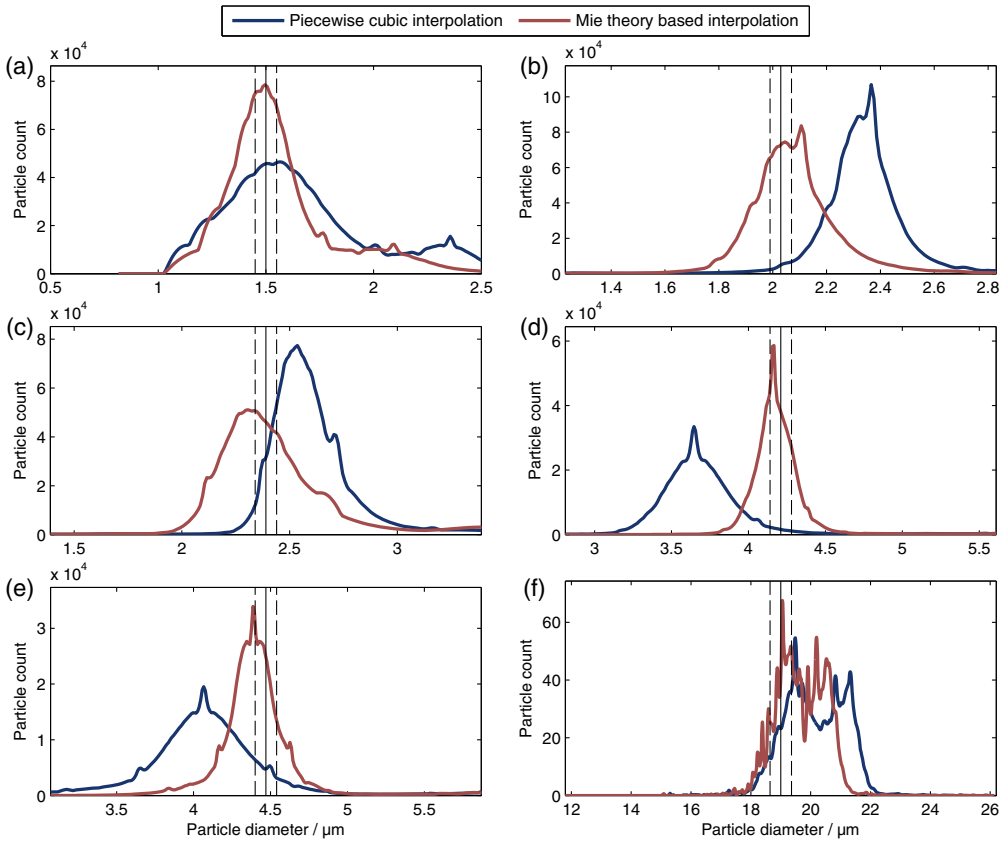

Fig. 7. Measurements of polystyrene microspheres are shown to evaluate the calibration improvement. Particle diameters obtained through piecewise cubic interpolation are shown in blue, while results making use of Mie-theory-based interpolation are depicted in red. The vertical black lines represent manufacturer information. The solid line stands for the center of the particle diameter distribution, and the dashed lines give the margin of error provided by the manufacturer. Shown particle sizes are (a) 1.50 µm, (b) 2.03 µm, (c) 2.39 µm, (d) 4.21 µm, (e) 4.47 µm, and (f) 19.30 µm.

Mie-theory-based interpolation yields fitting results. The most significant accuracy improvement is achieved for polystyrene particle sizes of 2.03, 4.21, and 4.47 μm, depicted in Figs. 7(b), 7(d), and 7(e). The size determination improvement for 1.50 μm particles, presented in Fig. 7(a), rather concerns the particle count than the determined particle sizes. Too small diameters below the actual particle size and too high diameters above render the resulting diameter distribution for piecewise cubic interpolation too wide and flat. With Mie-theory-based interpolation, the particle count inside the margin of error provided by the manufacturer is close to double the count using common interpolation methods. For polystyrene particle sizes 2.39 and 19.3 μm, depicted in Figs. 7(c) and 7(f), the results using Mie-theory-based interpolation yield only slightly better accordance with the manufacturer information than the results from piecewise cubic interpolation.

Polystyrene microspheres with a diameter of 4.21 μm from the same batch have been studied by our group before [18,19] using a scattering light microscope. There, the mean diameter of these particles was found to be closer to 4.15 than 4.21 μm. The overall tendency of the results for Mie-theory-based interpolation shows slightly lower mean particle sizes than described by the manufacturer information.

B. Measurements on Biological Samples Using PS Calibration

In the next step, particles with a different refractive indices compared to the calibration particles were measured. Figure 8(a) shows the analyzed data for THP-1 measurements. The particle size distribution obtained from both methods, neglecting the differing cell refractive index peaks around 4 to 5 μm. The use of Mie-theory-based interpolation with an assumed refractive index of 1.36, as discussed above, yields a high concentration of particles between 11 and 12 μm with a lower concentration of particles from 14 to 19 μm. These results are in good agreement with the phase contrast microscopy measurements, of which one exemplary image is presented in Fig. 8(b). Cell sizes from 10 to 18 μm have been determined from the phase contrast microscopy images. 10 μm sized cells and those from 16 to 18 μm were found rarely, and the highest population was found between 11 and 13 μm.

Similar good agreement is obtained applying Mie-theory-based interpolation to the CHO cell measurements, shown in Figs. 8(c) and 8(d), and yeast cell measurements, presented in Figs. 8(e) and 8(f). While simple interpolation results in particle sizes about half the actual cell diameters, Mie theory interpolation yields fitting results.

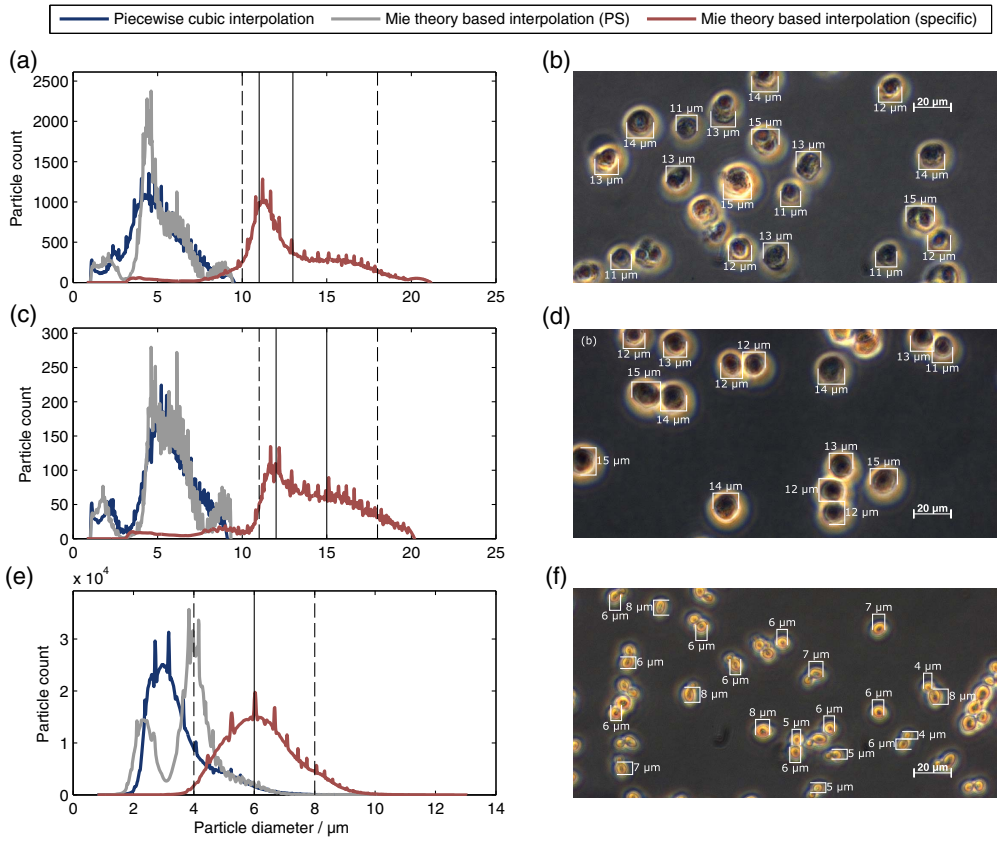

Fig. 8. Measurements of biological samples using polystyrene calibration. The left column of images compares piecewise cubic interpolation for a polystyrene calibration in blue with Mie-theory-based interpolation for polystyrene particles in gray and with regard to the individual refractive indices in red. The cell specific refractive indices are listed in Table 2. The images in the right column were taken with a phase contrast microscope and show exemplary cell sizes corresponding to their neighboring size distributions. Images (a) and (b) correspond to THP-1, (c) and (d) to CHO, and (e) and (f) to yeast cell measurements.

Mie-theory-based interpolation for optical particle counters examines one particle at a time with only one value measured, whereas many other methods using Mie theory either study an ensemble of particles or several distinct scattering angles simultaneously. Thus, other methods may achieve higher particle throughput at the cost of losing information of single particles or achieve higher particle characterization accuracy at the cost of a more complex and expensive setup. Where Mie-theory-based interpolation separates itself from most Mie-theory-based applications in the literature is in its applicability to commercially available devices that are already present in many laboratories, increasing their potential use without the need for physical adjustments of the setup.

Most limitations of Mie-theory-based interpolation derive from the particle counter used, such as measurable particle sizes, which are defined by the particle counter's SNR, sensor sensitivity, and data acquisition process. Limits to measurable particle concentrations are given by the particle counter sampling and flow rate, since coinciding particles in the detection volume have to be avoided. Particles that are edged or jagged and thereby cannot be approximated as a sphere can be assigned an equivalent diameter at best. Diameters of particles with significant absorption, on the other hand, should be determinable, since Mie theory handles complex refractive indices well.

5. CONCLUSION

Mie-theory-based interpolation has been proven a method to be able to increase the quality of particle counter calibration curves significantly. This can be used to further improve measurement results or decrease the amount of necessary calibration points, lowering time and financial burdens. Additionally, material specific calibration can be omitted, if the analyzed particles' refractive index is known. This approach is much faster and much less cost intensive than calibrations for each material that is to be analyzed. Therefore, Mie-theory-based interpolation in combination with a particle counter provides a tool for rapid particle counting and size determination, even for cells or other particles with the lack of a well fitting calibration material. The method can be used in a custom setup or a commercially obtained particle counter and can be adjusted to various detector designs.

An implementation of this method has been purchased by the particle counter manufacturer Markus Klotz GmbH and will be used for the calibration of particle counters, such as the Syringe, which was used as a test system in the presented work.

Acknowledgment. The authors thank the Markus Klotz GmbH for their cooperation, Dr. Rainer Wittig for the provision of the phase microscopy images, and Petra Kruse for the competent sample preparation.

REFERENCES

1. P. Aalto, K. Hämeri, P. Paatero, M. Kulmala, T. Bellander, N. Berglind, L. Bouso, G. Castano-Vinyals, J. Sunyer, G. Cattani, A. Marconi, J. Cyrys, S. von Klot, A. Peters, K. Zetzsche, T. Lanki, J. Pekkanen, F. Nyberg, B. Sjövall, and F. Forastiere, "Aerosol particle number concentration measurements in five European cities using TSI-3022 condensation particle counter over a three-year period during health effects of air pollution on susceptible subpopulations," J. Air Waste Manage. Assoc. **55**, 1064–1076 (2005).
2. A. J. Smolen, L. L. Wright, and T. J. Cunningham, "Neuron numbers in the superior cervical sympathetic ganglion of the rat: a critical comparison of methods for cell counting," J. Neurocytol. **12**, 739–750 (1983).
3. R. I. Amann, B. J. Binder, R. J. Olson, S. W. Chisholm, R. Devereux, and D. A. Stahl, "Combination of 16S rRNA-targeted oligonucleotide probes with flow cytometry for analyzing mixed microbial populations," Appl. Environ. Microbiol. **56**, 1919–1925 (1990).
4. J. Mäkelä, P. Aalto, V. Jokinen, T. Pohja, A. Nissinen, S. Palmroth, T. Markkanen, K. Seitsonen, H. Lihavainen, and M. Kulmala, "Observations of ultrafine aerosol particle formation and growth in boreal forest," Geophys. Res. Lett. **24**, 1219–1222 (1997).
5. J. Wu, R. Miller, D. Cooper, J. Flynn, D. Delson, and R. Teagle, "Deposition of submicron aerosol particles during integrated circuit manufacturing: experiments," J. Environ. Sci. **32**, 27–45 (1989).
6. J. L. Miller and D. Kitaljevich, "In-line oil debris monitor for aircraft engine condition assessment," in *IEEE Aerospace Conference Proceedings* (IEEE, 2000), Vol. **6**, pp. 49–56.
7. T. Bundschuh, R. Knopp, R. Winzenbacher, J. Il Kim, and R. Köster, "Quantification of aquatic nano particles after different steps of Bodensee water purification with laser-induced breakdown detection (LIBD)," Acta Hydrochim. Hydrobiol. **29**, 7–15 (2001).
8. S. Judd and P. Hillis, "Coagulation pretreatment for crossflow microfiltration of upland waters," Water Res. **35**, 2895–2904 (2001).
9. M. Akeson, D. Branton, J. J. Kasianowicz, E. Brandin, and D. W. Deamer, "Microsecond time-scale discrimination among polycytidylic acid, polyadenylic acid, and polyuridylic acid as homopolymers or as segments within single RNA molecules," Biophys. J. **77**, 3227–3233 (1999).
10. J. J. Kasianowicz, E. Brandin, D. Branton, and D. W. Deamer, "Characterization of individual polynucleotide molecules using a membrane channel," Proc. Natl. Acad. Sci. USA **93**, 13770–13773 (1996).
11. L. Sohn, O. Saleh, G. Facer, A. Beavis, R. Allan, and D. Notterman, "Capacitance cytometry: measuring biological cells one by one," Proc. Natl. Acad. Sci. USA **97**, 10687–10690 (2000).
12. J. Yarnell, I. Baker, P. Sweetnam, D. Bainton, J. O'Brien, P. Whitehead, and P. Elwood, "Fibrinogen, viscosity, and white blood cell count are major risk factors for ischemic heart disease. The Caerphilly and Speedwell collaborative heart disease studies," Circulation **83**, 836–844 (1991).
13. W. B. Kannel, K. Anderson, and P. W. Wilson, "White blood cell count and cardiovascular disease: insights from the Framingham study," J. Am. Med. Assoc. **267**, 1253–1256 (1992).
14. A. K. Burnett, D. Grimwade, E. Solomon, K. Wheatley, and A. H. Goldstone, "Presenting white blood cell count and kinetics of molecular remission predict prognosis in acute promyelocytic leukemia treated with all-trans retinoic acid: result of the randomized MRC trial," Blood **93**, 4131–4143 (1999).
15. B. Vozarova, N. Stefan, R. S. Lindsay, A. Saremi, R. E. Pratley, C. Bogardus, and P. A. Tataranni, "High alanine aminotransferase is associated with decreased hepatic insulin sensitivity and predicts the development of type 2 diabetes," Diabetes **51**, 1889–1895 (2002).
16. K. Pattanapanyasat and M. R. Thakar, "Cd4+ t cell count as a tool to monitor HIV progression & anti-retroviral therapy," Indian J. Med. Res. **121**, 539–549 (2005).
17. G. Mie, "Beiträge zur Optik Trüber Medien, Speziell Kolloidaler Metallösungen," Ann. Phys. **330**, 377–445 (1908).
18. M. Schmitz, T. Rothe, and A. Kienle, "Evaluation of a spectrally resolved scattering microscope," Biomed. Opt. Express **2**, 2665–2678 (2011).
19. T. Rothe, M. Schmitz, and A. Kienle, "Angular and spectrally resolved investigation of single particles by darkfield scattering microscopy," J. Biomed. Opt. **17**, 117006 (2012).
20. J. Stark, D. Müller, S. Nothelfer, and A. Kienle, "Angular and spectrally resolved investigations of yeast cells by light scattering microscopy and goniometric measurements," in *European Conference on Biomedical Optics* (Optical Society of America, 2015), paper 953718.

21. L. N. Lew, M. V. Ting, and T. C. Preston, "Determining the size and refractive index of homogeneous spherical aerosol particles using Mie resonance spectroscopy," Appl. Opt. **57**, 4601–4609 (2018).
22. G. B. de Boer, C. de Weerd, D. Thoenes, and H. W. Goossens, "Laser diffraction spectrometry: Fraunhofer diffraction versus Mie scattering," Part. Part. Syst. Charact. **4**, 14–19 (1987).
23. P. Chylek, V. Ramaswamy, A. Ashkin, and J. Dziedzic, "Simultaneous determination of refractive index and size of spherical dielectric particles from light scattering data," Appl. Opt. **22**, 2302–2307 (1983).
24. V. P. Maltsev, "Scanning flow cytometry for individual particle analysis," Rev. Sci. Instrum. **71**, 243–255 (2000).
25. L. Perelman, V. Backman, M. Wallace, G. Zonios, R. Manoharan, A. Nusrat, S. Shields, M. Seiler, C. Lima, T. Hamano, I. Itzkan, J. Van Dam, J. M. Crawford, and M. S. Feld, "Observation of periodic fine structure in reflectance from biological tissue: a new technique for measuring nuclear size distribution," Phys. Rev. Lett. **80**, 627–630 (1998).
26. A. Wax, C. Yang, V. Backman, K. Badizadegan, C. W. Boone, R. R. Dasari, and M. S. Feld, "Cellular organization and substructure measured using angle-resolved low-coherence interferometry," Biophys. J. **82**, 2256–2264 (2002).
27. C. F. Bohren and D. R. Huffman, *Absorption and Scattering of Light by Small Particles* (Wiley, 2008).
28. W. J. Wiscombe, "Improved Mie scattering algorithms," Appl. Opt. **19**, 1505–1509 (1980).
29. G. G. Stokes, "On the change of refrangibility of light," Philos. Trans. R. Soc. London **142**, 463–562 (1852).
30. E. Collett, "Mueller-Stokes matrix formulation of Fresnel's equations," Am. J. Phys. **39**, 517–528 (1971).
31. A. Savitzky and M. J. Golay, "Smoothing and differentiation of data by simplified least squares procedures," Anal. Chem. **36**, 1627–1639 (1964).
32. X. Liang, A. Liu, C. Lim, T. Ayi, and P. Yap, "Determining refractive index of single living cell using an integrated microchip," Sens. Actuators A Phys. **133**, 349–354 (2007).
33. W. Choi, C. Fang-Yen, K. Badizadegan, S. Oh, N. Lue, R. R. Dasari, and M. S. Feld, "Tomographic phase microscopy," Nat. Methods **4**, 717–719 (2007).
34. X. Su, M. Gupta, C. E. Capjack, Y. Y. Tsui, Y. Qiu, L. Marquez-Curtis, A. Janowska-Wieczorek, and W. Rozmus, "Label-free and noninvasive optical detection of the distribution of nanometer-size mitochondria in single cells," J. Biomed. Opt. **16**, 067003 (2011).
35. J.-W. Su, W.-C. Hsu, C.-Y. Chou, C.-H. Chang, and K.-B. Sung, "Digital holographic microtomography for high-resolution refractive index mapping of live cells," J. Biophoton. **6**, 416–424 (2013).
36. J. Stark, T. Rothe, S. Kieß, S. Simon, and A. Kienle, "Light scattering microscopy measurements of single nuclei compared with GPU-accelerated FDTD simulations," Phys. Med. Biol. **61**, 2749–2761 (2016).
37. S. Tsuchiya, M. Yamabe, Y. Yamaguchi, Y. Kobayashi, T. Konno, and K. Tada, "Establishment and characterization of a human acute monocytic leukemia cell line (THP-1)," Int. J. Cancer **26**, 171–176 (1980).